Lab on a Chip

RSCPublishing

Actively transporting virus like analytes with optofluidics for rapid and ultrasensitive biodetection†

Min Huang,[a] Betty C. Galarreta,[ab] Arif E. Cetin[a] and Hatice Altug*[ac]

Effective analyte delivery is essential to achieve rapid and sensitive biodetection systems. In this article, we present an actively controlled fluidic system integrated with a suspended plasmonic nanohole sensor to achieve superior analyte delivery efficiency and ultrafast sensor response, as compared to conventional fluidic systems. 70 nm sized virus like analyte solution is used to experimentally demonstrate the system performance improvements. Sensor response time is reduced by one order of magnitude as compared to the conventional methods. A seven orders of magnitude dynamic concentration range from 10^3 to 10^9 particles mL^{-1} is quantified, corresponding to a concentration window relevant to clinical diagnosis and drug screening. Our non-destructive detection system, by enabling efficient analyte delivery, fast sensing response and minimal sample volume, opens up opportunities for sensitive, rapid and real-time virus detection in infectious disease control and point-of-care applications.

Introduction

Rapid and precise detection of infectious viruses in environmental or clinical samples is important to efficiently prevent disease outbreaks and spreading. Traditional methods such as plaque assay are time consuming and labor intensive. Plaque formation can take 3–14 days, depending on the virus being analyzed.[1,2] Modern methods include enzyme-linked immunosorbent assays (ELISA) and polymerase chain reaction (PCR). ELISA technique requires multiple steps and takes 4 to 24 hours incubation time.[3,4] In addition, it lacks the ability to detect analytes in real time and limited for use outside the laboratory settings. Real time PCR takes around 1 to 4 hours and can provide quantitative result of virus at low concentration.[5,6] However, it requires advanced laboratory equipment and trained personnel for significant sample preparation. Therefore, there is a need for a rapid, accurate and easy-to-use system that allows real-time and point-of-care detection of viruses. Surface-based biosensors are emerging as promising diagnostic systems for this purpose.[7–12] Irrespective of signal transduction mechanisms (optical,[13–16] electrical,[17–19] mechanical[20–22]), surface bionsensors require immobilizing receptors on the surface to selectively bind the analytes of interest in solution. The analyte binding event relies on two factors: chemical reaction and analyte delivery. Chemical reaction determines how the receptors and the analytes interact with each other and reach equilibrium. Reaction rates are intrinsic properties of the receptor-analyte system and difficult to change. The second factor, analyte delivery, plays an equally important role as it directly controls the amount of analytes that can be captured by the immobilized receptors on the sensing surface. To improve delivery efficiency of the analytes to the sensor, concurrently researchers are integrating surface biosensors with microfluidics.[23–30] While microfluidics can enable lab-on-a-chip systems, recent theoretical and numerical calculations indicate that we have to take careful consideration in the design of the fluidic cell.[31–33] Significantly, for nanosensors embedded in conventional microfluidic channels, the performance is limited in a fluidic environment by inefficient analyte transport.[34,35] In a typical microfluidic system, analytes are transported to the sensing area by convection and diffusion. However, diffusion rates decrease as the analyte sizes increase. For example, analytes larger than 50 nm (typical size for majority of infectious viruses) have difficulties being efficiently transported to the sensor. Moreover, as the analytes are collected by the functionalized sensor surface, depletion zone forms.[29,36] The depletion zone is a region where only a few analytes are available around the sensing area. For samples with diluted concentrations, the inefficient analyte transport would require impractically long detection time. Increasing the flow rate can improve the convective transport and deliver more analytes. However, the effect is minor as the total mass transport depends weakly on the flow rate.[37] Furthermore, increasing the flow rate significantly increases the required sample volume and causes excessive analyte consumption.

[a] Electrical and Computer Engineering Department, Boston University, Boston, MA, USA

[b] Departamento de Ciencias-Quimica, Pontificia Universidad Catolica del Peru, Lima, Peru

[c] Bioengineering Department, Ecole Polytechnique Federale de Lausanne, Lausanne, Switzerland. E-mail: Hatice.altug@epfl.ch

To improve the analyte transportation efficiency, in our previous works we demonstrated a proof-of-concept biosensing system merging nanophotonics and nanofluidics in a single platform.[38,39] Unlike conventional approaches where the analytes simply flow over the surface (Fig. 1a), our platform enables active delivery of the analytes onto the sensor. The system consists of a suspended plasmonic nanohole sensor sealed between two microfluidic channels. Inlet for the solution is in the upper channel while outlet is in the bottom channel (Fig. 1b). The analyte solution is actively steered through the nanohole openings and then flows to the bottom channel.

In this work, we experimentally and theoretically demonstrate that the actively controlled flow scheme significantly improves sensor performance as compared to the conventional flow method. Particularly, we demonstrate that the proposed scheme is beneficial when detecting analytes with relatively large dimensions. Our calculations, scaling analysis and finite element simulation, show that actively controlled flow scheme can reduce the sensor response time by one order of magnitude for particles of 70 nm size and two orders of magnitude for particles of 700 nm, when compared with the conventional flow method. Performance of the system is studied experimentally by detecting analytes of 70 nm diameter mimicking the behaviour of similar size viruses. Dynamic range over seven orders of magnitude starting from 10^3 particles mL^{-1} is quantified using our actively controlled flow scheme. This broad range covers concentrations relevant to most clinical applications. Significantly, sensor response time is reduced by an order of magnitude from 4 hours to 30 minutes, thus enabling real-time detection for rapid diagnosis. In addition, the virus like analytes are detected intact

from small sample volumes. Therefore, we provide a rapid, nondestructive, ultrasensitive and real time biosensing system for clinical and field-oriented point-of-care applications.

Superior analyte transport efficiency by actively controlled flow scheme

To develop a physically intuitive and practical understanding of the benefits of actively controlled flow scheme over the conventional method, we perform analytical calculations on both schemes. The performance of flow systems is evaluated by the channel Peclet number, the mass transport flux and the Damkohler number. The first two parameters are related to the analyte transport effect. The Peclet number, defined as the ratio of particles transported onto the sensing surface by convection over diffusion, determines the size of the depletion zone. Larger Peclet number means a smaller fraction of the analytes is delivered onto the sensing area. The mass transport flux represents the total number of analytes transported to the sensor per unit time for interaction with the bound receptors. The Damkohler number, defined as the ratio of reactive to diffusive flux, takes the binding kinetics effect into consideration. If Damkohler number is much larger than 1, mass transport is limiting, indicating that there are not enough analytes transported onto the sensor for interaction. If this number is much smaller than 1, on the other hand, the chemical reaction is too slow to interact with the fast analyte flux. A detailed explanation on these parameters can be found in the supplementary information.

For the conventional flow model we consider a sensor of width $W_s = 60$ μm and length $L_s = 60$ μm, is placed in a micro-channel of height $H_c = 100$ μm and width $W_c = 100$ μm, as shown in Fig. 1a. A solution of analytes with concentration $c_0 = 100$ nM and diffusivity $D = 7$ μm^2 s^{-1}, (a typical diffusivity for 70 nm radius particles in water) is assumed to flow with rate $Q = 5$ μL min^{-1}. The sensor is modeled as a flat square instead of nanohole arrays for simplicity. Using analytical calculations from Squires, et al.,[31] we obtain the channel Peclet number as 1.2×10^5. This large number indicates that the diffusion time is much longer than the convection time. Therefore, the depletion zone is much thinner than the channel height, and most of the analytes would go through the channel instead of diffusing towards the sensor. The mass transport flux is calculated to be 1.1 molecules s^{-1}, meaning only one analyte can be delivered onto the sensor surface every second by mass transport. The total amount of analytes captured by the sensor may be further lowered by binding kinetics. Herein, the binding constants are assumed to be $k_{on} = 7 \times 10^7$ M^{-1} and $k_{off} = 3 \times 10^{-6}$ s^{-1}.[40] The binding site density on the sensor surface is $b_0 = 2 \times 10^{12}$ sites m^{-2} (Fig. 1b). We calculate the Damkohler number for this conventional flow model to be 60, showing that chemical binding process is instantaneous as compared to the time needed for analyte to be transported to the sensing surface. Therefore, this system is working in an analyte transport limited condition.
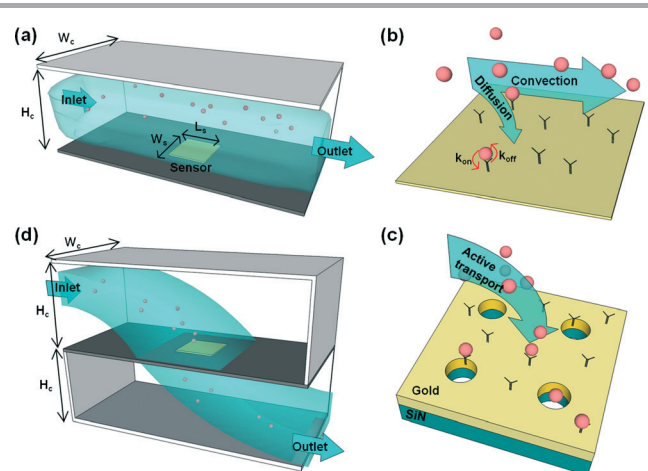
Fig. 1 Schematics of the conventional and the actively controlled flow schemes. (a) Illustration of the conventional flow scheme. Solution flows through a microfluidic channel of height H_c and width W_c. The sensor of length L_s and width W_s is placed in the channel. (b) Zoom-in image of the functionalized sensing surface. The association and dissociation constants of the receptor-analyte system are k_{on} and k_{off}, respectively. (c) Illustration of actively controlled flow scheme. The plasmonic nanohole sensor is placed between two channels. All the other parameters are the same as the conventional flow scheme. (d) Zoom-in image of a 2 × 2 nanohole array shows analytes flowing from one channel to the other through the nanoholes.

The actively controlled flow system is modeled as a suspended nanohole array sensor being placed between two flow channels, as shown in Fig. 1c. The channel geometry, the sensor size, the fluidic parameters and the binding kinetic constants are assumed to be the same as in the conventional flow scheme. The sensing surface is a nanohole array patterned on a 100 nm thick silicon nitride (Si_3N_4) layer with a 100 nm gold layer (Fig. 1d). Nanoholes are D_{hole} = 200 nm in diameter and P = 600 nm in period. As a result, there are $N_{hole} = 10^4$ nanoholes on the sensor. Analyte solution passes from one channel to the other through the nanohole array. Therefore the flow rate through each nanohole is 5×10^{-4} μL min^{-1} (Q/N_{hole}). For simplicity, the sensing area is taken as the gold side wall of the holes (colored in orange in Fig. 1d). For this scheme, we calculate the channel Peclet number as 4×10^3, which is almost two orders of magnitude smaller than for the conventional method. This value indicates that more analytes will be transported towards the sensing surface. The total mass transport flux calculated (60 molecules s^{-1}) is nearly 60 times more than for the conventional scheme. The Damkohler number calculated in this case is 0.2, meaning that the sensor operates neither in a reaction limited nor a diffusion limited regime.

These analytical calculations suggest that the proposed flow scheme enables active delivery of analytes towards the sensing surface and overcomes the mass transport limitation. As a result, the sensitivity and detection time of the biosensor can be significantly improved. These results are further strengthened with finite element simulations (COMSOL Multiphysics®) in the following section.

Evaluation of sensor performance in active and conventional flow scheme when detecting analytes with different dimensions

To quantitatively study the actively controlled and the conventional flow scheme, we apply finite element method for both schemes. The simulations are divided in three parts. First, the steady state velocity distribution is calculated to show the convection effect in the flow channels. Then, analyte concentration in solution is calculated at the equilibrium point to illustrate the depletion zones and the analyte delivery efficiency. Finally, the total amount of analytes accumulated on the sensing surface as a function of time is investigated for analytes with different sizes to evaluate the sensor performance.

To determine steady state flow profile for both flow schemes, Navier–Stokes equation that describes the motion of fluid is solved in a 2D model (see supplementary information for details). Herein, microfluidic channels are scaled down to 20 μm in length and 5 μm in height in order to reduce the time for numerical calculation. Nanohole sensors in both schemes are represented by 20 apertures. In the conventional scheme, the holes are modeled with closed ends, while for the actively controlled flow scheme suspended

nanoholes are open ended enabling solution to flow. The analyte solution is injected into the chamber from the inlet with a flow rate of 5×10^{-4} m s^{-1}. Velocity distributions for both conventional and actively controlled flow schemes are shown in Fig. 2. For better illustration, we also plot arrow lines to show the flow direction; and arrow length represents the flow rate. We observe the formation of laminar flow profile for the conventional flow scheme. The convective flow is fast on the center of the channel but becomes very slow near the edges as shown in the zoom-in image of Fig. 2a. In the proposed flow scheme, solution is steered directly towards the sensing surface (Fig. 2b). Strong convective flow is observed around the sensing surface (Fig. 2b, zoom-in image), suggesting that active flow can strongly improve the delivery of analytes onto the sensor surface.

Once the steady state flow profiles within the channels are calculated for both schemes, the analyte concentration is determined by solving the analyte transport equation. This equation considers the convection and diffusion of the analytes in the channel and the analyte binding kinetics with receptors on the sensing surface. Detailed information about the simulation is given in the supplementary information. Fig. 3 shows the analyte concentration in solution at equilibrium. Here the sensing surface is assumed to capture the analytes immediately and never saturates, so that the binding kinetic issue is excluded and only the mass transport effect is considered. For the conventional scheme (Fig. 3a), analyte concentration is extremely low at the sensing surface and the calculated depletion zone is 1/8 of the channel height. Analyte solution away from the depletion zone is highly concentrated and flow faster (Fig. 2a). As a result, most of the analytes are swept over the sensor without reaching to the sensing surface for interaction. On the contrary, in the actively controlled flow method (Fig. 3b), all the analytes are guided towards the nanohole sensing area. Most of the
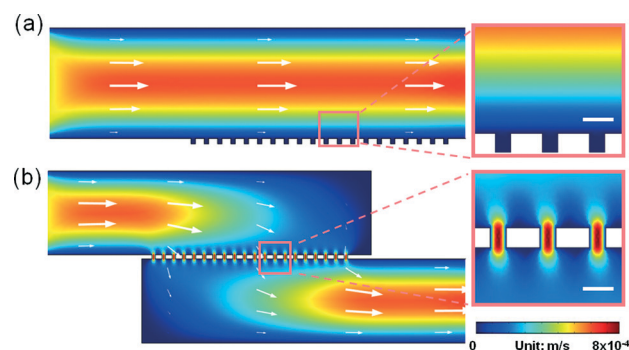

Fig. 2 Steady state velocity distribution for the conventional and the actively controlled flow schemes. (a) Flow velocity distribution for conventional flow scheme is presented in color scheme and arrow lines. Color bar depicts the flow rate distribution of the solution. White arrows indicate the direction of the flow and their sizes represent the flow rate. Laminar flow is formed inside the channel. Zoom-in image shows the flow around the nanohole sensor in detail. (b) Flow velocity distribution for actively controlled flow scheme. Analyte solution is steered through the hole array and flows to the bottom channel. Zoom-in image shows the flow is strong around the apertures. Scale bars in zoom-in images represent 400 nm.
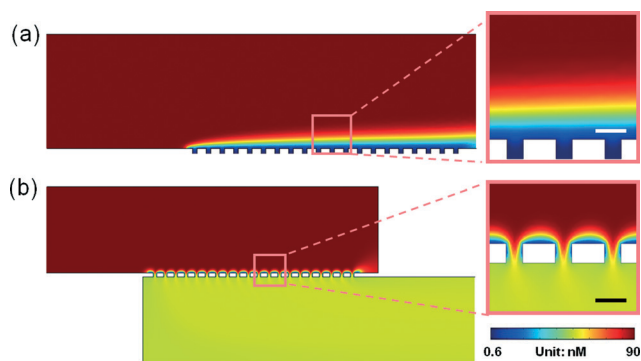
Fig. 3 Analyte concentration in the conventional and the actively controlled flow schemes. (a) Analyte concentration in the conventional flow scheme. Zoom-in image shows that depletion zone is form on top of the sensor and most of the analytes do not reach to the sensing area. Color bar on the bottom right indicates the concentration gradient of the analytes in solution. (b) Illustration of analyte concentration in the actively controlled flow scheme. Zoom-in image shows that the depletion zone shrinks around the nanohole openings. Thus majority of analytes are transported to the sensing area. Scale bar in zoomed-in images represents 400 nm.

analytes are captured by the receptors on the sensing surface as the depletion zone shrinks around the nanohole openings.

In reality, binding kinetics has the effect of slowing down the sensor response and the chemical reaction reaches equilibrium eventually. With this effect taken into account, we can now calculate the sensor response time, *i.e.* time the system needs to reach equilibrium and evaluate the performance of both schemes. In comparison to the analysis of Fig. 3, here the first order Langmuir boundary condition is used. Inset in Fig. 4 shows analyte accumulation on the sensor surface as a function of time for both schemes when the diffusion rate of the analyte is 70 μm^2 s^{-1}. The sensor response time for the conventional flow scheme is 60 min (blue dash line), while it is 4 times faster (16 min) for the
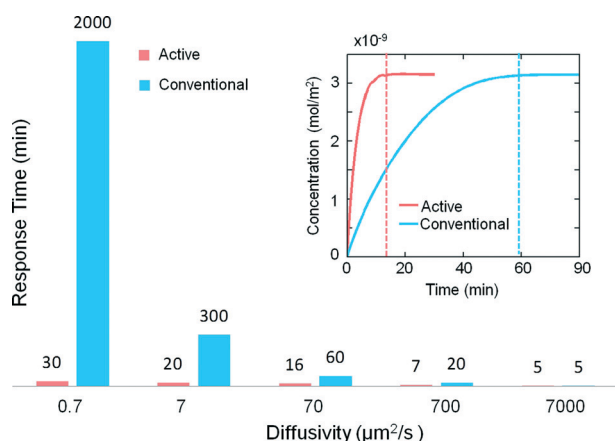

Fig. 4 Calculated sensor response time for analytes with different diffusivities for conventional (blue) and actively controlled (red) flow schemes. The performance of the conventional flow scheme dramatically declines as the analyte diffusivity increases (analyte size increases). Inset shows the amount of analyte captured by a sensor as a function of time for both flow schemes when the analyte diffusivity is 70 μm^2 s^{-1}. Red and blue dash lines indicate when the reaction reaches equilibrium for each flow scheme.

actively controlled flow scheme (red dash line). Since analyte diffusivity is a function of particle size, we further evaluate the performance of both flow methods by studying analytes with different diffusivities. Fig. 4 shows the sensor response time for analytes with diffusion rates ranging from 0.7 μm^2 s^{-1} to 7000 μm^2 s^{-1}. For the conventional flow scheme (blue bars) the response time becomes extremely slower as the analytes diffuse slower. Particularly, the sensor response time is nearly two orders of magnitude slower when the diffusivity is 0.7 μm^2 s^{-1} as compared to the active flow scheme. On the contrary, for the actively controlled flow scheme (red bars), the sensor response time increases only 6 times (from 5 min to 30 min) as the analyte diffusivity becomes 4 orders of magnitude larger. Correspondingly, sensor in actively controlled flow scheme is barely affected by the analyte diffusivity. Given that bigger particles have smaller diffusivities, it is evident that the actively controlled flow scheme is beneficial when detecting analytes of large sizes such as viruses.

Rapid and ultrasensitive detection of virus like analytes by the actively controlled method

In this section, we experimentally demonstrate that the actively controlled flow method yields better sensing performance than the conventional flow scheme. Our detection platform is based on extraordinary optical transmission (EOT) phenomenon[41] in suspended plasmonic nanohole arrays.[42,43] The device consists of suspended nanohole gratings that can couple the normally incident light to surface plasmons,[44–48] *i.e.* charge oscillations confined at metal/dielectric interface. In our system both surface propagating plasmons (SPP) and localized surface plasmons (LSP) are excited. The SPP resonance has field component mainly at the top metal surface, while LSPs have inside and near the rims of the nanoholes. The resonance wavelength is strongly dependent on the dielectric constant of the medium around the structure. As the analytes bind to these areas, the effective refractive index of the medium increases and the plasmonic resonance wavelength red shifts. As a result, *in situ* detection of the analyte bindings on the sensor surface and inside the nanoholes can be achieved quantitatively and in a label free fashion. In our design, the nanoholes are 200 nm in diameter and separated by 600 nm, supporting spectrally sharp EOT resonances in aqueous medium at near-infrared wavelengths. Fabrication of these nanohole structures is achieved by using deep ultraviolet (DUV) lithography. Compared to the most common nanopatterning techniques such as electron beam lithography (EBL), DUV enables low cost and time effective fabrication at wafer scales. A 4-inch wafer yields 52 sensor chips of 1 cm by 1 cm in size. For our sensor design, each chip contains 3 by 3 nanohole arrays and each array is 100 μm by 100 μm. Transmission spectra of these structures are comparable to that of the arrays fabricated by EBL (see ESI† for details).
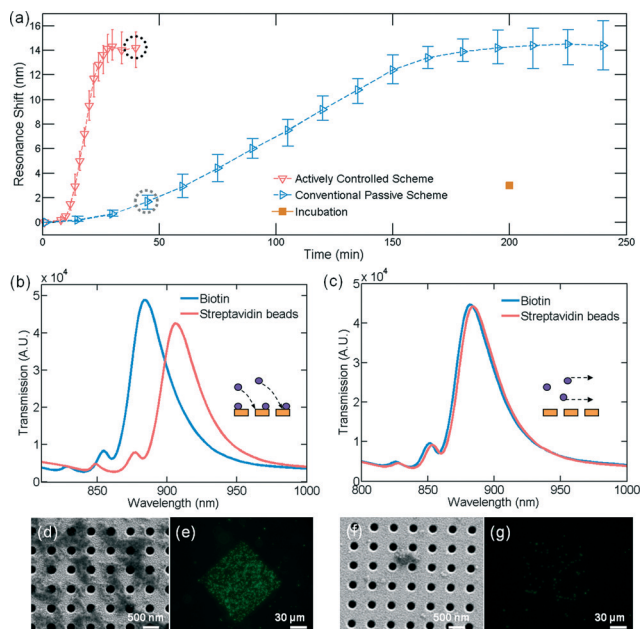
In the experimental setup (Fig. 5a) the sensor chip is first functionalized with biotinylated thiol (NanoScience Instruments)
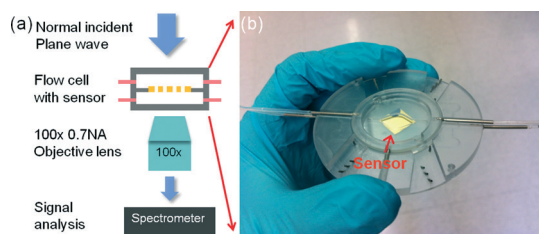
Fig. 5 Experimental setup for detection of virus like analytes with active transportation. (a) Schematic view of the experimental setup is presented. The EOT resonance is excited by launching a normally incident light. The transmitted signal is then collected for spectral analysis. (b) Image of the customized flow cell with sensor is shown. The plasmonic nanohole sensor is sealed between two microfluidic channels. The inlet/outlet in the channels can be manipulated to realize conventional or actively controlled flow scheme.

Fig. 6 Sensor response for the conventional and the actively controlled flow scheme when detecting functionalized bead solution at 10^7 particles mL^{-1}. (a) Real time sensor responses of different flow schemes for 10^7 particles mL^{-1} streptavidin coated bead solution are shown. Plot shows resonance shifts with respect to the reference as a function of time. Sensor reaches equilibrium ~10 times faster in the actively controlled flow system as compared to the conventional system. The orange data point shows 3-nm resonance shift resulted from traditional incubation method. (b), (c) Transmission spectra of the sensor in the actively controlled flow scheme and conventional flow scheme are shown, respectively. Blue curves show the spectra obtained when the biotin functionalized sensors are immersed in PBS, at time zero. Red curves show the spectra recorded at ~40 min, as indicated by circles in (a). At this time point, 15 nm and 2 nm resonance shifts are observed for the actively controlled and conventional flow scheme, respectively. (d), (f) SEM images of the sensors for the actively controlled and conventional cases at ~40 min are shown, respectively. (e), (g) Fluorescent images of the sensors for the actively controlled and conventional cases show the presence of the beads captured on the sensor surfaces.

at a concentration of 0.5 mM in ethanol overnight. Then, sensor is cleaned twice with ethanol for 5 minutes each time, followed by water for another 5 minutes and blow dried with nitrogen. After functionalization process, the sensor is embedded in a customized chamber with two inlets/outlets both on the top and the bottom channels (Fig. 5b). The flow chamber is placed on an inverted microscope and the transmission spectrum of the sensor is obtained by launching a collimated and unpolarized light at normal incidence. The transmitted signal is collected with a 100×0.7 numerical aperture objective lens and fiber coupled into a spectrometer for spectral analysis. To implement the conventional flow scheme, where the convective flow is parallel to the surface, we block the inlet/outlet of the bottom channel. To steer the convective flow actively towards the sensing surface, we block one of the openings of the both channels. In both cases, the chamber is filled with PBS (10 mM phosphate buffer solution at physiological pH), and the transmission spectrum is used as reference. 70-nm sized polystyrene beads coated with streptavidin (Spherotech) are used as analytes to mimic viruses of comparable size. Bead solution is then pumped into the chamber at a flow rate of 5 μL min^{-1}. These streptavidin coated beads are transported onto the sensor and captured by the biotinylated sensing surface. As a result, we can monitor the binding events by measuring the red shift of the resonance wavelength with respect to the reference.

The resonance red-shifts as a function of time for both flow schemes are shown in Fig. 6a. Sensor in the actively controlled flow chamber reaches equilibrium in less than 25 minutes (red curve). Instead, it takes nearly 4 hours for the sensor to be saturated in the conventional flow chamber (blue curve). These measurements clearly demonstrate that the sensor response time is reduced by one order of magnitude for the proposed flow scheme. Furthermore, we perform an experiment using traditional incubation method (no flow involved). The sensor is placed in a sealed petri dish with bead solution coating its surface. Only 3 nm resonance shift is observed after 3.5 hours incubation, as shown in Fig. 6a (orange point), indicating extremely poor analyte transport efficiency. Fig. 6b & 6c show the spectra of the sensors in both flow schemes after ~40 minutes (highlighted with circles

in Fig. 6a). At this time point the sensor with the actively controlled flow reaches equilibrium, and about 15 nm resonance shift is observed (Fig. 6b). On the contrary, only 2 nm shift is detected for the sensor in the conventional flow scheme (Fig. 6c). SEM images of the sensors are taken to confirm the binding events. In the actively controlled flow case, large amounts of beads are immobilized on the sensor surface (Fig. 6d), while for the conventional scheme only a few beads are observed (Fig. 6f). The results are further confirmed by fluorescent measurements. A 1.5 nM solution of biotin-fluorescein (Thermo Fisher Scientific-Pierce) in PBS is incubated for 30 min on the sensor after the streptavidin coated beads are bound on the surface and washed with PBS. The sensor of size 100×100 μm is captured within the field of view of fluorescence microscopy images (Fig. 6e & 6g). For the actively controlled flow scheme, a strong fluorescent signal is observed mainly on the nanohole areas (Fig. 6e). Almost no fluorescence is detected on the sensor embedded in a conventional flow scheme (Fig. 6g). These results show that the actively controlled flow scheme promotes the transport of
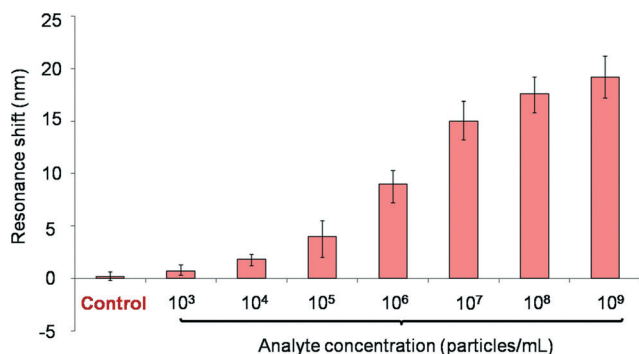
Fig. 7 Quantitative measurements of 70-nm sized streptavidin coated beads at different concentrations (10^3–10^9 particles mL^{-1}). Control represents the reaction between non-biotinylated sensor and 10^7 particles mL^{-1} analyte solution. Error bars are obtained from 4 independent experiments at each concentration.

analytes to the sensor and dramatically reduces the sensor response time. Additionally, analytes are guided effectively to the sensing area. The amount of analytes adsorbed outside the sensor resulting in no signal is significantly reduced.

Given the fact that actively controlled flow method dramatically improves the sensor response, we investigate the detection limit of our system as well as its repeatability using 70-nm sized streptavidin coated beads (Fig. 7). Bead solutions at seven different concentrations, ranging from 10^3 to 10^9 particles mL^{-1} and separated by one order of magnitude, are evaluated using the actively controlled flow scheme. A non-biotinylated sensor surface is taken as the control, in which case interaction with the beads should be minimal or zero. At least four independent experiments have been done for each concentration. In each experiment, the chamber is first filled with PBS, and the resonance wavelength is taken as reference. Then, the sample solution is injected at a flow rate of 5 μL min^{-1} and the resonance shifts are recorded after equilibrium (Fig. 7). For the control experiments, resonance shift less than 0.5 nm is observed, indicating minimal non-specific binding between the surface and the analytes. A concentration curve is obtained over seven orders of magnitude. Resonance shifts are reproducible at each concentration and quantitative measurements are achieved. Notably, diluted samples with a concentration as low as 10^3 particles mL^{-1} show 1 nm shift on average, which is clearly distinguishable compared to the control sensors. Given that a detection limit of 10^7 PFU mL^{-1} is usually sufficient for clinical applications, our platform has the potential for rapid and sensitive clinical diagnosis.

Conclusions

This work presents a compact optofluidic biosensing platform for ultrasensitive, rapid, quantitative and label-free detection of virus like analytes. The proposed actively controlled flow method can effectively guide the analytes towards the sensing area, resulting in superior sensor responses. Experiments using 70-nm sized virus like analytes demonstrate that sensor response time is reduced by one order of magnitude for samples at clinically relevant concentrations,

indicating that tests could be performed in real time and diagnosis could be made in less than an hour for most clinical studies using our system. Detection of seven orders of magnitude dynamic concentration range (10^3–10^9 particles mL^{-1}) is demonstrated on this fluidic biosensing platform. This detection range is sufficient for most clinical applications. In addition, virus like analytes are captured and detected intact without being damaged, so that the samples could be used for further studies. Furthermore, we demonstrate for the first time DUV lithography to fabricate plasmonic biosensors. DUV enables wafer scale high throughput manufacturing at low cost, enabling point-of-care systems particularly suitable for developing countries.

Acknowledgements

Notes and references

1 M. Kramski, A. Drozd, G. F. Lichtfuss, P. W. Dabrowski and H. Ellerbrok, *Virol. J.*, 2011, **8**, 1–7.
2 R. L. DeBiasi and K. L. Tyler, *Clin. Microbiol. Rev.*, 2004, **17**, 903–925.
3 D. K. Kim and B. Poudel, *Yonsei Med. J.*, 2013, **54**, 560–566.
4 J. Wagoner, *et al. Hepatology*, 2010, **51**, 1912–1921.
5 V. M. Corman, *et al. Euro Surveill.*, 2012, **17**, 20285.
6 S. Chevaliez, *et al. Hepatology*, 2007, **46**, 22–31.
7 X. Fan, *et al. Anal. Chim. Acta*, 2008, **620**, 8–26.
8 X. D. Hoa, A. G. Kirk and M. Tabrizian, *Biosens. Bioelectron.*, 2007, **23**, 151–160.
9 M. Moskovits, *J. Raman Spectrosc.*, 2005, **36**, 485–496.
10 R. Quidant and M. Kreuzer, *Nat. Nanotechnol.*, 2010, **5**, 762–763.
11 M. Pla-Roca, *et al. Mol. Cell. Proteomics*, 2012, **11**, M111.011460.
12 A. Pallaoro, G. B. Braun and M. Moskovits, *Proc. Natl. Acad. Sci. U. S. A.*, 2011, **108**, 16559–16564.
13 C. L. Chang, Z. Ding, V. N. Patchigolla, B. Ziaie and C. Savran, *IEEE Sens. J.*, 2012, **12**, 2374–2379.
14 J. C. Reed, H. Zhu, A. Y. Zhu, C. Li and E. Cubukcu, *Nano Lett.*, 2012, **12**, 4090–4094.
15 N. Liu, M. Mesch, T. Weiss, M. Hentschel and H. Giessen, *Nano Lett.*, 2010, **10**, 2342–2348.
16 C. Wu, *et al. Nat. Mater.*, 2011, **11**, 69–75.
17 Y. Shao, *et al. Electroanalysis*, 2010, **22**, 1027–1036.
18 S. Roy and Z. Gao, *Nano Today*, 2009, **4**, 318–334.
19 A. De Leebeeck, *et al. Anal. Chem.*, 2007, **79**, 4094–4100.
20 A. Gahlmann, *et al. Nano Lett.*, 2013, **13**, 987–993.
21 K. Icoz and C. Savran, *Appl. Phys. Lett.*, 2010, **97**, 123701–123701.
22 L. G. Carrascosa, *et al. TrAC, Trends Anal. Chem.*, 2006, **25**, 196–206.

23 N. V. Zaytseva, *et al. Lab Chip*, 2005, **5**, 805–811.

24 A. Bange, H. B. Halsall and W. R. Heineman, *Biosens. Bioelectron.*, 2005, **20**, 2488–2503.

25 S. Moon, H. O. Keles, A. Ozcan, A. Khademhosseini, E. Hæggstrom, D. Kuritzkes and U. Demirci, *Biosens. Bioelectron.*, 2009, **24**, 3208–3214.

26 M. G. von Muhlen, N. D. Brault, S. M. Knudsen, S. Jiang and S. R. Manalis, *Anal. Chem.*, 2010, **82**, 1905–1910.

27 P. S. Dittrich and A. Manz, *Nat. Rev. Drug Discovery*, 2006, **5**, 210–218.

28 M. A. Qasaimeh, S. G. Ricoult and D. Juncker, *Lab Chip*, 2013, **13**, 40–50.

29 P. Sethu, A. Sin and M. Toner, *Lab Chip*, 2006, **6**, 83–89.

30 C. B. Rohde, F. Zeng, R. Gonzalez-Rubio, M. Angel and M. F. Yanik, *Proc. Natl. Acad. Sci. U. S. A.*, 2007, **104**, 13891–1389.

31 T. M. Squires, R. J. Messinger and S. R. Manalis, *Nat. Biotechnol.*, 2008, **26**, 417–426.

32 P. E. Sheehan and L. J. Whitman, *Nano Lett.*, 2005, **5**, 803–807.

33 G. Hu, Y. Gao and D. Li, *Biosens. Bioelectron.*, 2007, **22**, 1403–1409.

34 D. R. Kim and X. Zheng, *Nano Lett.*, 2008, **8**, 3233–3237.

35 P. R. Nair and M. A. Alam, *Appl. Phys. Lett.*, 2006, **88**, 233120–233120.

36 O. Hofmann, G. Voirin, P. Niedermann and A. Manz, *Anal. Chem.*, 2002, **74**, 5243–5250.

37 J. Newman, *Electroanal. Chem.*, 1973, **6**, 279–297.

38 M. Huang, *et al. Opt. Express*, 2009, **17**, 24224–24233.

39 A. A. Yanik, *et al. Appl. Phys. Lett.*, 2010, **96**, 021101–021101.

40 M. H. Qureshi, *et al. J. Biol. Chem.*, 2001, **49**, 46422–46428.

41 J. Braun, B. Gompf, T. Weiss, H. Giessen, M. Dressel and U. Hübner, *Phys. Rev. B*, 2011, **84**, 155419.

42 A. A. Yanik, *et al. Nano Lett.*, 2010, **10**, 4962–4969.

43 A. A. Yanik, *et al. Proc. Natl. Acad. Sci. U. S. A.*, 2011, **108**, 11784–11789.

44 E. Ozbay, *Science*, 2006, **311**, 189–193.

45 R. Zia, *et al. Mater. Today*, 2006, **9**, 20–27.

46 P. B. Catrysse, G. Veronis, H. Shin, J. T. Shen and S. Fan, *Appl. Phys. Lett.*, 2006, **88**, 031101–031101.

47 B. Luk'yanchuk, N. I. Zheludev, S. A. Maier, N. J. Halas, P. Nordlander, H. Giessen and C. T. Chong, *Nat. Mater.*, 2010, **9**, 707–715.

48 A. V. Kabashin, *Nat. Mater.*, 2009, **8**, 867–871.